Review

Orbits of Particles and Photons around Regular Rotating Black Holes and Solitons

Irina Dymnikova and Anna Dobosz

Review

Orbits of Particles and Photons around Regular Rotating Black Holes and Solitons

Irina Dymnikova [1,*] and **Anna Dobosz** [1,2]

[1] Department of Mathematical Physics and Applied Mathematics, A.F. Ioffe Physico-Technical Institute of the Russian Academy of Sciences, Polytekhnicheskaja 26, St. Petersburg 194021, Russia

[2] Department of Mathematics and Computer Science, University of Warmia and Mazury, Słoneczna 54, 10-710 Olsztyn, Poland

[*] Correspondence: igd.ammp@mail.ioffe.ru or irina@uwm.edu.pl; Tel.: +7-812-292-7912

Abstract: We briefly overview the basic properties and generic behavior of circular equatorial particle orbits and light rings around regular rotating compact objects with dark energy interiors, which are described by regular metrics of the Kerr–Schild class and include rotating black holes and self-gravitating spinning solitons replacing naked singularities. These objects have an internal de Sitter vacuum disk and can have two types of dark interiors, depending on the energy conditions. The first type reduces to the de Sitter disk, the second contains a closed de Sitter surface and an $\mathcal{S}$ surface with the de Sitter disk as the bridge and an anisotropic phantom fluid in the regions between the $\mathcal{S}$ surface and the disk. In regular geometry, the potentials decrease from $V(r) \to \infty$ to their minima, which ensures the existence of the innermost stable photon and particle orbits that are essential for processes of energy extraction occurring within the ergoregions, which for the second type of interiors contain the phantom energy. The innermost orbits provide a diagnostic tool for investigation of dark interiors of de Sitter–Kerr objects. They include light rings which confine these objects and ensure the most informative observational signature for rotating black holes presented by their shadows.

Keywords: de Sitter–Kerr black hole; de Sitter–Kerr soliton; the innermost orbits; light rings; black hole shadows

1. Introduction

Astronomical data persistently testify that our universe is dominated by about 75% dark energy, described by the equation of the state $p = w\rho$ with $w < -1/3$, which guarantees accelerated expansion. The best fit, $w = -1$ [1,2], represents the cosmological constant λ, corresponding to the vacuum density $\rho_{vac} = (8\pi G)^{-1}\lambda$.

The dominant role of a cosmic dark energy, $p = -\rho$, $\rho = (8\pi G)^{-1}\Lambda$, responsible for the first inflation in the universe's evolution [3], as well as for a non-zero cosmological constant today [2,4,5], was confirmed by the CMB measurements [6] combined with baryon acoustic oscillations (BAOs) data [1] and Ia-type supernovae (SNe) data [7,8], which gave the current value $w = -1.06 \pm 0.06$ at 68% CL [1,2], where w is the equation of the state parameter in $w = p/\rho$.

Dark energy models in modified gravity theories were reviewed in [9] for the $f(R)$, $f(G)$ and $f(R, G)$ gravity, for modified gravity with nonlinear gravitational coupling and string-inspired theory with Gauss–Bonnet dilaton coupling in the late universe, where they lead to accelerated expansion. A detailed review of $f(R)$ theories is presented in [10], and the history of the universe's evolution in modified gravity is presented in [11].

Various dark energy models have been developed, describing evolution between a large value of the cosmological constant, required by the first inflation, and its small presently observed value ([2,12]) and the references therein).

Model-independent analysis of a dark energy evolution based on the BAO data [1] distinguished theories in which the cosmological constant Λ relaxes from a large initial value [13].

In our papers, we studied the relaxation of the cosmological constant, including the initial, final and intermediate (if necessary) de Sitter stages [14–19], in the frame of the model-independent, self-consistent approach, which introduces vacuum dark energy in a general setting on the basis of the algebraic classification of the stress–energy tensors responsible for the spacetime symmetry and allows for an intrinsically variable cosmological constant [20,21].

Remarkably, a similar story with Λ relaxation occurs within regular compact objects with de Sitter vacuum interiors. These include regular black holes, their remnants and self-gravitating solitons called G-lumps (replacing naked singularities), which are non-singular, non-dissipative compact objects without horizons [21,22] classified as physical solitons in accordance with the definition of Coleman lumps [23] (for a review, see [24]).

The key point is that although the quantum field theory does not contain an appropriate symmetry to vanish the cosmological vacuum density ρ or to reduce it to a certain non-zero value ([17,25] and the references therein), such a symmetry does exist as the spacetime symmetry, provided by the algebraic structure of stress–energy tensors, which determine the spacetime geometry as the source terms in Einstein equations.

The algebraic classification of stress–energy tensors [26,27] allows for a model-independent definition of a vacuum as a medium by the algebraic structure of its stress–energy tensor [20,28] and admits the existence of vacua whose symmetries are reduced in comparison with the maximally symmetric de Sitter vacuum $T_k^i = \rho_{vac}\delta_k^i$ ($p = -\rho_{vac}$; $\rho_{vac} = $ const by $T_{k;i}^i = 0$). A vacuum with a reduced symmetry [20,28] keeps the Lorentz invariance in certain spatial directions ($p_\alpha = -\rho$; $\alpha = 1, 2$), presents an anisotropic vacuum's dark fluid [21] and describes an anisotropic vacuum's dark energy, which evolves over time and is spatially inhomogeneous, by virtue of $T_{k;i}^i = 0$. In the spherically symmetric case, its stress–energy tensor has the algebraic structure

$$T_0^0 = T_1^1 \tag{1}$$

where $T_0^0 = \rho$; $T_1^1 = p_r = -\rho$; $T_2^2 = T_3^3 = p_\perp = -\rho - r\rho'/2$ and the dynamical cosmological constant is presented by its variable T_0^0 component [20].

The spherically symmetric solutions to the Einstein equations with stress–energy tensors specified by Equation (1) and satisfying the weak energy condition (WEC), which ensures a positive energy density for any local observer, dependent on the coordinate mapping or cosmological models, describe regular compact objects with Λ relaxing from the de Sitter vacuum and spacetime symmetry changing from the de Sitter group.

The mass of these objects $M = 4\pi \int_0^\infty \rho(r)r^2 dr$ is related to the de Sitter vacuum and breaking of the spacetime symmetry from the de Sitter group [29,30], and it can be presented as $M = (4\pi/3)\rho_0 r_0^2 r_g = (4\pi/3)\rho_0 r_s^3$, where $r_g = 2GM$, $\rho_0 = \rho(r \to 0)$ and $r_0 = (3/(8\pi G\rho_0))^{1/2}$. The length scale $r_s = (r_0^2 r_g)^{1/3}$ is characteristic for the de Sitter–Schwarzschild geometry, matching the Schwarzschild exterior to the de Sitter interior directly [31] or continuously [28].

The underlying hypotheses predict the appearance of a de Sitter vacuum instead of a singularity as a result of self-regulation of the geometry by vacuum polarization effects [31], of achieving the limiting curvature at the Planck scale [32], and of symmetry restoration for the de Sitter group at the GUT scale (as the process reverses to symmetry breaking), which prevents formation of a singularity under negative de Sitter pressure [28,33]. Formation of the de Sitter core in place of the Schwarzschild singularity was reported in the frame of the loop quantum gravity [34,35], renormalization group improvement [36] and non-commutative geometry [37].

Spherical solutions specified by Equation (1) belong to the Kerr–Shild class [38] and can be transformed to axially symmetric solutions by the general approach developed by Gürses and Gürsey [39], which includes the Newman–Janis algorithm [40] and is usually applied for obtaining regular solutions which describe rotating black holes [41–50] (for

a reccent review, see [51]). The de Sitter center becomes the equatorial de Sitter vacuum disk, which is the generic constituent of all regular rotating black holes and spinning solitons [51–54].

Energy conditions distinguish two types of dark interiors for regular rotating de Sitter–Kerr compact objects [55]. The first reduces to the de Sitter vacuum disk and satisfies the WEC. The second type contains a two-dimensional closed version of the de Sitter vacuum, called the $\mathcal{S}$ surface, with the de Sitter disk as a bridge. The regions between the $\mathcal{S}$ surface and the disk contain a phantom energy and violate the WEC [51,54]. Phantom energy, originally introduced by the equation of the state $p + \rho < 0$ [56] (for a review, see [57]), in the case of rotating objects with the second type of interior, is intrinsically anisotropic, where $p_r = -\rho$; $p_\perp + \rho < 0$ [55].

The geometry of rotating black holes contains the ergosphere, which confines the ergoregion where the mechanism extracts the rotational energy (for a topical review, see [58]). For the regular de Sitter–Kerr geometry, we expect that the processes of energy extraction would involve an additional vacuum and phantom energy [53,54]. A spinning soliton can have two ergospheres and an ergoregion between them or one ergosphere and an ergoregion beyond it [54]. For solitons with the second type of interior, a phantom region is not screened by the event horizon, which strongly facilitates extraction of phantom energy [54,55].

In this paper, we briefly overview the circular equatorial orbits around de Sitter–Kerr objects with special attention directed toward the innermost orbits, which can be involved in the processes of energy extraction from their ergoregions and are essential for their observational signatures.

The innermost circular particle orbits around regular rotating black holes were presented for two particular solutions with an electric and magnetic charge in [59,60]. Time-like and null geodesics for the Hayward black hole [61] are presented in [62], and the difference in particle orbits from those for the Kerr black hole is considered in [63].

A systematic study of spherical orbits around the Kerr black hole was presented in [64]. The conditions for existence of the stable circular and spherical orbits, including the innermost stable circular orbits and marginally stable spherical orbits, for charged particles in the Kerr–Newman spacetime with cloud strings, quintessence and an electromagnetic field were studied in detail in [65]. The motion of charged particles in the field of deformed Schwarzschild black holes with external magnetic fields in modified theories of gravity was studied in [66]. The chaotic motion of a charged particle in the magnetized modified Schwarzschild spacetime was analyzed in [67], where it was shown that the chaos strengthens with an increasing modified gravity parameter and weakens with increasing particle angular momentum [67]. In [68], it was shown that chaos for charged particles is facilitated in the accelerated universe, namely in the Reissner–Nordström–de Sitter spacetime, but does not occur in the Reissner–Nordström anti-de Sitter spacetime. In [69], the authors compared the stable circular orbits and innermost stable circular orbits of charged particles for a Balart–Vagenas regular black hole [44] and a Reissner–Nordström black hole, and they showed that the differences are relatively minor.

The spherical photon orbits around a Kerr black hole were presented in [70], while those for Kerr-like black holes were presented in [71], and those for extreme Kerr–Newman–AdS black holes were presented in [72]. Stable photon orbits in stationary, axially symmetric electrovacuum spacetimes were studied in [73]. The question of stability of the light rings around spherical compact objects was addressed in [74,75], and that for the axially symmetric case was addressed in [76–79].

In our paper [80], we carried out general analysis and classification of the equatorial circular orbits around de Sitter–Kerr compact objects, including detailed analysis of the innermost orbits, which provided a diagnostic tool for investigation of their dark interiors. We studied, in general, the settings for the typical behavior and locations of the light rings, formed by closed photon orbits responsible for such informative observational signatures of a black hole as its shadow, and showed that all compact de Sitter–Kerr objects can be

classified as ultra-compact objects [80], defined as the self-gravitating structures confined by the light rings ([77,81] and the references therein).

Section 2 presents the internal structure of de Sitter–Kerr black holes and solitons. In Section 3, we overview the circular equatorial particle orbits and light rings, including detailed information about the innermost orbits. Section 4 is devoted to the observational signatures of de Sitter–Kerr compact objects related to their GUT interiors, as well as the observational signatures of de Sitter–Kerr black holes provided by the shadows formed by the innermost photon orbits. Section 5 contains the conclusions.

2. Internal Structure of de Sitter–Kerr Compact Objects

The regular solutions to the Einstein equations include the axially symmetric solutions obtained from the spherically symmetric solutions of the Kerr–Schild class, which are specified by the algebraic structure of their source terms (Equation (1)) and described by the metric [38]

$$ds^2 = g(r)dt^2 - g(r)^{-1}gr^2 - r^2 d\Omega^2; \ \ g(r) = 1 - \frac{2G\mathcal{M}(r)}{r}; \ \ \mathcal{M}(r) = 4\pi \int_0^r \tilde{\rho}(x)x^2 dx \quad (2)$$

where $\tilde{\rho}(r)$ is a spherical density profile. All regular spherical solutions of the Kerr–Schild class have the de Sitter centers if their source terms (Equation (1)) satisfy the WEC [29,82].

The spherical solutions of the Kerr–Shild class (Equation (2)) are transformed to the axially symmetric solutions while applying the Gürses–Gürsey approach [39] based on the complex Trautman–Newman translations, which include the Newman–Janis algorithm that is usually applied for constructing new axially symmetric solutions (for a review, see [51]). In the Boyer–Lindquist coordinates and in the geometrical units $c = G = 1$, the axially symmetric metric reads as follows [39]:

$$ds^2 = \frac{2f - \Sigma}{\Sigma} dt^2 + \frac{\Sigma}{\Delta} dr^2 + \Sigma d\theta^2 - \frac{4af\sin^2\theta}{\Sigma} dt d\phi + \left(r^2 + a^2 + \frac{2fa^2\sin^2\theta}{\Sigma}\right)\sin^2\theta d\phi^2 \quad (3)$$

$$\Delta = r^2 + a^2 - 2f(r); \ \ f(r) = r\mathcal{M}(r); \ \ \Sigma = r^2 + a^2 \cos^2\theta \quad (4)$$

where a is the specific angular momentum. The Boyer–Lindquist coordinates are related to the Cartesian coordinates x, y, z by $x^2 + y^2 = (r^2 + a^2)\sin^2\theta; \ z = r\cos\theta$. The master function $f(r) = r\mathcal{M}(r)$, relating an axial solution with an original spherical solution, tends to be in the limit from $r \to \infty$ to $f(r) \to Mr$ and describes the Kerr metric. The mass parameter $M = 4\pi \int_0^\infty \tilde{\rho}(r)r^2 dr$ comes from a spherical solution and is related to breaking the spacetime symmetry from the de Sitter group in the origin [29,52]. For $r \to 0$, the master function behaves as $f(r) = r^4 / 2r_0^2; \ r_0^2 = 3/8\pi\tilde{\rho}(0)$ and represents the de Sitter metric. The dimensionless parameter which characterizes the Sitter–Kerr compact object is $x_g = r_g/r_0$.

In the axially symmetric geometry, the surfaces of a constant r are the confocal ellipsoids:

$$r^4 - (x^2 + y^2 + z^2 - a^2)r^2 - a^2 z^2 = 0. \quad (5)$$

For $r = 0$, these ellipsoids degenerate to the equatorial disk [83]:

$$x^2 + y^2 \leq a^2, \ \ z = 0. \quad (6)$$

The de Sitter–Kerr spacetime can have at most two horizons defined by $\Delta(r_+, r_-) = 0$:

$$r_{+,-} = \mathcal{M}(r) \pm \sqrt{\mathcal{M}^2 - a^2}; \ \ r_\pm = \mathcal{M}(r_\pm) \quad (7)$$

where r_+ is the event horizon, $r_- < r_+$ is the internal Cauchy horizon, and $r_\pm$ is the double horizon of the extreme black hole with $a = a_{dh} = \mathcal{M}(r_\pm) = r_\pm$ [53,54].

The ergospheres are defined by $g_{tt} = r_e^2 + a^2 \cos^2 \theta - 2f(r_e) = 0$, having confined ergoregions with $g_{tt} < 0$, which provides the possibility of energy extraction. Black holes have one ergosphere and ergoregion above the event horizon r_+. Solitons can have one ergoregion between two ergospheres or one ergosphere and ergoregion involving the whole interior [54].

The density $\rho(r, \theta)$, radial pressure p_r, and transversal pressure $p_\perp(r, \theta)$ (eigenvalues of a stress–energy tensor in the co-rotating frame with the angular velocity $\omega(r) = u^\phi/u^t = a/(r^2 + a^2)$) present an intrinsically anisotropic dark fluid [21,54]:

$$\rho(r, \theta) = \frac{r^4}{\Sigma^2} \tilde{\rho}(r); \quad p_r = -\rho; \quad p_\perp(r, \theta) = \left(\frac{r^4}{\Sigma^2} - \frac{2r^2}{\Sigma} \right) \tilde{\rho}(r) - \frac{r^3}{2\Sigma} \tilde{\rho}'(r). \tag{8}$$

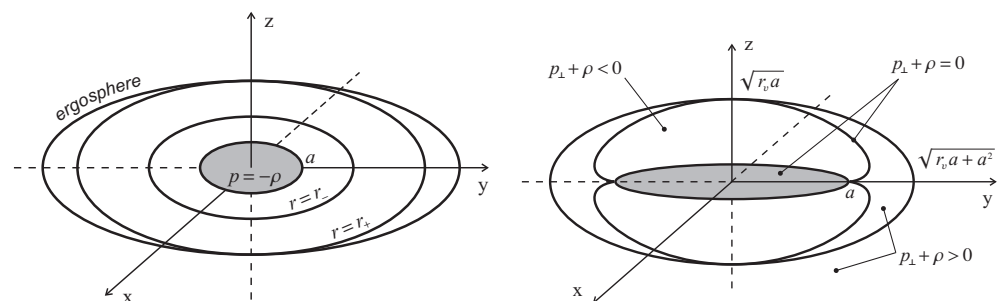On the equatorial disk in Equation (6), the equation of the state takes the form

$$p_\perp = p_r = -\rho \tag{9}$$

and describes the de Sitter vacuum $p = -\rho$ in the co-rotating frame.

Equation (8) gives the basic relation for investigation of the deep interiors of de Sitter–Kerr objects, depending on the energy conditions [53,54]:

$$p_r = -\rho: \quad p_\perp + \rho = \frac{r|\tilde{\rho}'|}{2\Sigma^2} \mathcal{S}(r, z); \quad \mathcal{S}(r, z) = r^4 - z^2 P(r); \quad P(r) = \frac{2a^2}{r|\tilde{\rho}'|}(\tilde{\rho} - \tilde{p_\perp}). \tag{10}$$

If an original spherical solution violates the dominant energy condition (DEC), which requires $\rho \geq p_\alpha$, then an axial solution satisfies the WEC (which requires $\rho + p_\alpha \geq 0$), and the deep interior is presented by the de Sitter vacuum disk [53,54]. The first type of interior is shown in Figure 1 (left) together with the horizons and the ergosphere [54].

Figure 1. The first type of interior, horizons, and ergosphere (**left**) and second type of interior (**right**).

If a spherical solution satisfies the DEC, then an axial solution contains an additional closed de Sitter surface ($\mathcal{S}$ surface) with the de Sitter disk as the bridge [53]. In the regions between the $\mathcal{S}$ surface and the disk, the WEC is violated ($p_\perp + \rho < 0$), which is identified as a phantom fluid with $p_\perp < -\rho$ [54] (for a review, see [51,84]). The second type of interior is shown in Figure 1 (right) [54], where r_v is a model-dependent regularization parameter [54]. The location of the $\mathcal{S}$ surface with respect to the ergospheres, depending on the basic parameter $x_g = r_g/r_0$, is shown in Figure 2 [80] for two values of the angular momentum a.

In the soliton field, with an increase in its angular momentum a above a certain value dependent on the density profile, the ergoregion, open for a distant observer, includes increasing parts of the phantom region, which provides the mechanism for extraction of phantom energy in addition to the rotational energy [53,54].
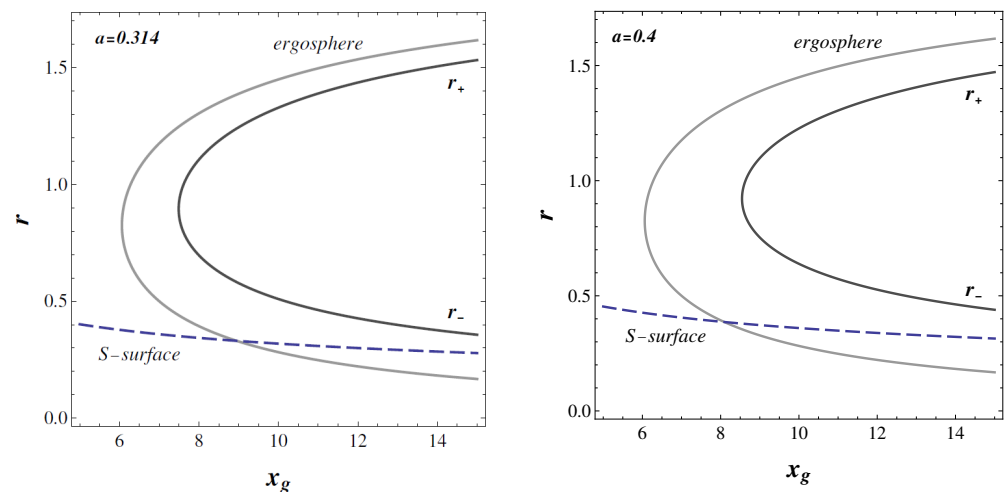
Figure 2. $\mathcal{S}$ surface, horizons, and ergospheres for $a = 0.314$ (**left**) and $a = 0.4$ (**right**).

3. Circular Equatorial Orbits and Light Rings

In regular geometry, the potentials decrease from $V(r) \to \infty$ to $r \to 0$, which provides the existence of the innermost stable orbits for particles and photons in their first minima.

The behavior and characteristics of orbits depending on a have been studied by analysis of the curves $r(a)$ defined parametrically by the orbit equations as $f(r, a) = 0$ [80].

3.1. Particle Orbits

The particle orbits are described by the equation — for time-like geodesics [83]:

$$\dot{r}^2 = E^2 - V_p(r); \quad V_p(r) = \frac{\Delta}{r^2} - \frac{2\mathcal{M}}{r^3}(L - aE)^2 + \frac{(L^2 - a^2 E^2)}{r^2} \tag{11}$$

where E and L are the integrals of motion on the orbit: the energy and the projection of the angular momentum on the $z-$axis, respectively. The potential V_p decreases as a^2/r^2.

Marginally bound orbits are the limiting orbits defined by $E^2 = 1$ [83]. The innermost stable and direct marginally bound orbits exist in the minima of the potentials ($V_p' = 0$), described by [80]

$$\mathcal{M}r^2 + \mathcal{M}'r^3 - 4\mathcal{M}^2 r - a^2(\mathcal{M} - \mathcal{M}'r) \mp 4a\mathcal{M}\sqrt{\mathcal{M}r - \mathcal{M}'r^2} = 0 \tag{12}$$

where an upper sign refers to the retrograde orbits and the lower sign to the direct orbits.

By differentiating the orbit equation (Equation (12)) with respect to r and a, we find the equation for a curve $r(a)$ which determines the behavior and characteristics of orbits: [80]

$$[(\mathcal{M} - \mathcal{M}'r)(8\mathcal{M}r - r^2) - 4a(2\mathcal{M}r - \mathcal{M}'r^2)\sqrt{\mathcal{M}/r - \mathcal{M}'}$$

$$-\frac{2a\mathcal{M}(\mathcal{M} - \mathcal{M}'r + \mathcal{M}''r^2)}{\sqrt{\mathcal{M}/r - \mathcal{M}'}} + 3a^2(\mathcal{M} - \mathcal{M}'r) + a^2\mathcal{M}''r^2 + \mathcal{M}''r^4]dr$$

$$= -r[4\mathcal{M}\sqrt{\mathcal{M} - \mathcal{M}'r} - 2a(\mathcal{M} - \mathcal{M}'r)]da. \tag{13}$$
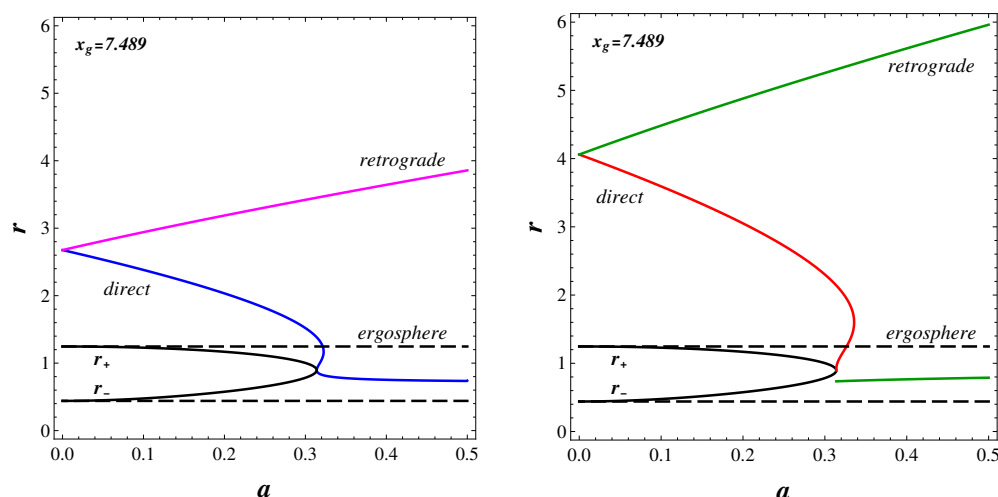
Detailed analysis of the curve $r(a)$ [80] showed that the innermost stable, marginally bound orbits approach the branching point on the double horizon $r = r_\pm$ from the soliton region with $dr/da < 0$ and $a > a_{dh}$. At the stable orbit $r = r_\pm$, the curve $r(a)$ changes its direction to $dr/da > 0$ and continues along the additional branch of stable orbits unless it meets the next branching point, which is the degenerate orbit ($V'' = 0$), where it changes the direction to $dr/da < 0$ and continues on the branch of unstable orbits with an increasing radius r, which should have (and has) the same behavior as the Kerr orbits, where $dr/da < 0$ [83]. The marginally bound orbits are shown in Figure 3 (left) [80].

Marginally stable orbits satisfy the equation $V' = V'' = 0$ and form the next group of limiting orbits. Analysis of their behavior has been studied by applying the orbit equation in terms of the metric function $g(r) = 1 - 2G\mathcal{M}(r)/r$, which reads as follows [80]:

$$a^2(rg'' - g') \mp 8arg'\sqrt{rg'/2} + r^3gg'' + 3r^2gg' - 2r^3g'^2 = 0. \tag{14}$$

An upper sign in Equation (14) refers to the retrograde orbits, while a lower sign refers to the direct orbits. Detailed analysis of Equation (14) has shown that there are no direct innermost orbits with $dr/da < 0$ in the soliton region with $a > a_{dh}$ and $r < r_\pm$. Instead, in this region, there exist the retrograde innermost orbits.

The branch of direct, marginally stable orbits begins on the double horizon, which is the degenerate ($V'' = 0$) orbit $r = r_\pm$ at $a = a_{dh}$ which continues in the soliton region with $r > r_\pm$, $a > a_{dh}$, and $dr/da > 0$ and goes toward a branching point $r_{br\,ms} > r_\pm$ at $a_{br\,ms} > a_{dh}$, where it changes its direction to $dr/da < 0$ and then follows the asymptotic Kerr branch with $dr/da < 0$. Marginally stable orbits are shown in Figure 3 (right) [80].

Figure 3. Dependence of radii on a for the marginally bound orbits (**left**) and for the marginally stable orbits (**right**), where $x_g = r_g/r_0$.

3.2. Light Rings

Closed photon orbits are described by the null geodesics: [80]

$$\dot{r}^2 = E^2 - V_\gamma(r) = 0; \quad V_\gamma(r) = -\frac{2\mathcal{M}(r)}{r^3}(L - aE)^2 + \frac{(L^2 - a^2E^2)}{r^2}. \tag{15}$$

The potentials $V_\gamma(r)$ in the regular geometry essentially behave different from those in the Kerr geometry; they decrease from $V_\gamma(r) \to \infty$ to $r \to 0$, which ensures the existence of the innermost stable orbits in their first minima.

Light rings are presented by the closed photon orbits, which are determined by the zeros of the potential derivative [80]:

$$V_\gamma'(r) = \left[-\frac{2}{r^3}(L^2 - a^2E^2) + \frac{6\mathcal{M}(r)}{r^4}(L - aE)^2 - \frac{2\mathcal{M}'(r)}{r^3}(L - aE)^2 \right] = 0. \tag{16}$$

Equations (15) and (16) allow one to express the integrals of motion E and L as dependent on the radius r and obtain the general equation which governs the photons' orbits [80]:

$$r^{3/2} + \mathcal{M}'r^{3/2} - 3\mathcal{M}r^{1/2} \mp 2a\sqrt{\mathcal{M} - \mathcal{M}'r} = 0 \tag{17}$$
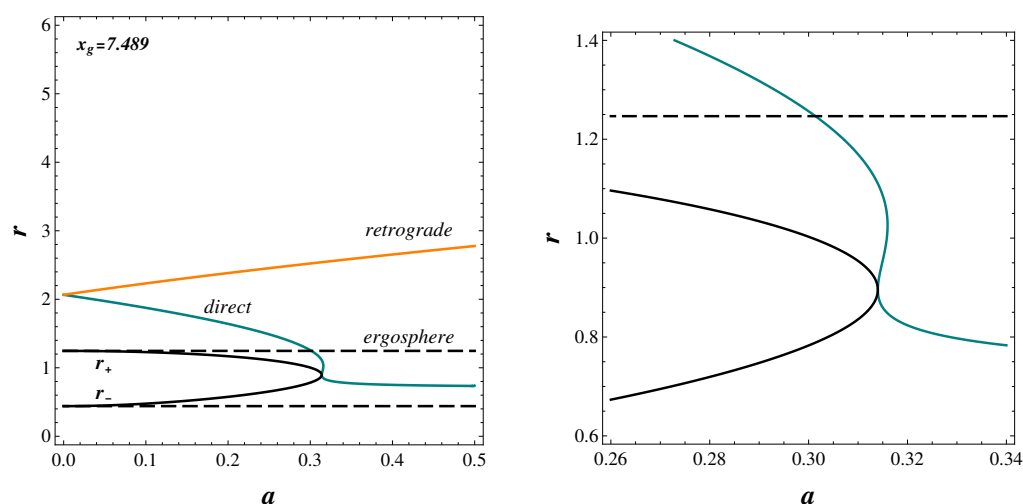
where an upper sign corresponds to a retrograde orbit (counter-rotating light ring) and a lower sign corresponds to a direct orbit (co-rotating light ring). For $\mathcal{M} = M = const$, this equation coincides with the relevant equation in the Kerr metric [83].

The behavior and characteristics of orbits have been studied by detailed analysis of the curve $r(a)$, defined parametrically by the orbit with Equation (17), which gives the following basic equation [80]:

$$\frac{dr}{da} = -\frac{4\sqrt{\mathcal{M}r - \mathcal{M}'r^2}}{3\Delta' + 4\mathcal{M}''r^2 - (4a\mathcal{M}''r^2)/(\sqrt{\mathcal{M}r - \mathcal{M}'r^2})}. \tag{18}$$

For direct orbits, the curve $r(a)$ has two branching points, with the first on the double horizon $r_{\pm}$ for $a = a_{dh}$ and the next at $r_{br\gamma} > r_{\pm}$ for $a_{br\gamma} > a_{dh}$. In the black hole region ($a \leq a_{dh}$), there exists one branch of unstable retrograde orbits with $dr/da > 0$ and one branch of direct orbits with $dr/da < 0$, which can be stable or unstable depending on the density profile (mass function). In the soliton region, for $a_{dh} < a < a_{br\gamma}$, there are three branches of direct orbits and one branch of retrograde orbits. For $a = a_{br\gamma}$, there are two direct orbits and one retrograde orbit. For $a > a_{br\gamma}$, there are the innermost stable direct orbits and unstable retrograde orbits. The existence of light rings around de Sitter–Kerr black holes and spinning solitons identifies them as ultra-compact objects defined as self-gravitating objects with light rings [81]. The light rings are shown in Figure 4 (left), and their enlarged image in the vicinity of the double horizon is shown in Figure 4 (right) [80].

Figure 4. Photon orbits, horizons, and ergospheres depending on a (**left**) and their enlarged image near the double horizon (**right**), where $x_g = r_g/r_0$.
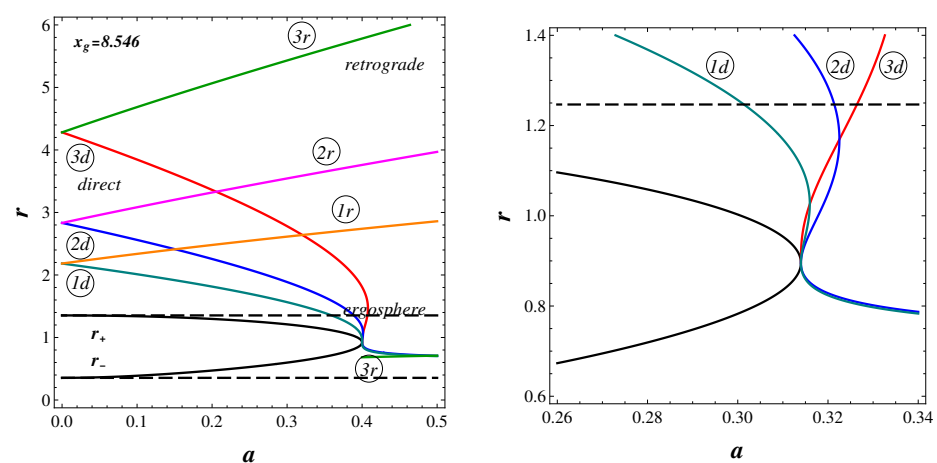
Around the soliton, for $a > a_{dh}$, there were three co-rotating light rings: the innermost stable light ring, the additional co-rotating light rings, which were stable or unstable depending on the density profile, and the degenerate ($V_\gamma(r)'' = 0$) co-rotating light rings on the way to the asymptotic Kerr branch of unstable light rings. Appearing here in a natural fashion were degenerate light rings (transitional between stable and unstable orbits), which confirmed the prediction in [74] for the existence of degenerate light rings for a certain class of spherical ultra-compact objects, and this was extended to the general axially symmetric case of regular de Sitter–Kerr ultra-compact objects [80].

3.3. All Limiting Orbits

Three limiting orbits include the innermost particle orbits (marginally stable and marginally bound) as well as the innermost proton orbits. All of them exist as direct innermost orbits on the double horizon $r = r_{\pm}$ at $a = a_{dh}$, which is the branching point on the curves $r(a)$ for the photon orbits and marginally bound orbits, where they change

their directions from $dr/da < 0$ to $dr/da > 0$. Marginally stable innermost direct orbits with $r < r_\pm$ do not exist for $a > a_{dh}$; instead, they begin on the double horizon $r = r_\pm$. The innermost marginally stable orbits in this range of parameters are presented by the branch of retrograde orbits, which starts at a certain value $r < r_\pm$ with $dr/da > 0$ and continues with r increasing very slowly as a increases [80]. All the innermost direct orbits, after leaving $r = r_\pm$, arrive at their branching points, which are $r_{br\ \gamma} > r_{dh}$ for the photon orbit, $r_{br\ mb} > r_{br\ \gamma}$ for the marginally bound orbits, and $r_{br\ ms} > r_{br\ mb}$ for the marginally stable orbit. Each of them changes in direction from $dr/da > 0$ to $dr/da < 0$ and arrives at the asymptotically Kerr branches of unstable direct orbits.

In Figure 5 [80], we show all the innermost orbits (left) and an enlarged image of the direct innermost orbits in the vicinity of the double horizon (right). The photon orbits are marked with (1), the marginally bound particle orbit is marked with (2), and the marginally stable orbit is marked with (3).

Figure 5. Limiting orbits in the de Sitter–Kerr geometry depending on a (**left**) and an enlarged image near the double horizon (**right**), where $x_g = r_g/r_0$.

Pictures illustrating the generic properties of the geometries and behavior of orbits have been plotted for the exact axially symmetric solution [53,54], which were obtained from the spherical solution with the phenomenologically regularized Newtonian profile [54]:

$$\tilde{\rho} = \frac{B^2}{(r^2 + r_v^2)^2}; \quad r_v = \frac{\pi^2 B^2}{M}; \quad B^2 = \tilde{\rho}_0 r_v^4; \quad r_v = \left(\frac{4 r_0^2 r_g}{3\pi}\right)^{1/3} = \left(\frac{4}{3\pi}\right)^{1/3} r_s \quad (19)$$

where $r_s = (r_0^2 r_g)^{1/3}$ is the characteristic length scale for geometries with the de Sitter interiors. The sperical metric function $g(r)$ and the mass function $\mathcal{M}(r)$ are [54]

$$g(r) = 1 - \frac{2 r_g}{\pi r}\left(\arctan\frac{r}{r_v} - \frac{r r_v}{r^2 + r_v^2}\right); \quad \mathcal{M}(r) = \frac{r_g}{\pi}\left(\arctan\frac{r}{r_v} - \frac{r r_v}{r^2 + r_v^2}\right). \quad (20)$$

The regularization scale r_v is directly related to the zero-gravity surface at which the strong energy condition is violated and the gravitational acceleration becomes repulsive, where $\tilde{\rho} + \sum_k \tilde{p}_k = 0 \rightarrow \tilde{\rho}_0 r_v^4 (r^2 - r_v^2)/(r^2 + r_v^2)^3 = 0$.

4. Observational Signatures

Primordial regular black holes, their remnants, and self-gravitating solitons are considered heavy dark matter candidates [85] which are generically related to dark energy due to their de Sitter and phantom interiors (for a review, see [24]). Their specific observational signatures are provided by their de Sitter vacuum interiors. At the GUT energy scale, the baryon and lepton numbers are not conserved, and this can lead to induced proton decay

in an underground detector. In the 1 km^3 detector, as in the IceCUBE, one can expect up to 300 events per year [85].

Particles and photons on the innermost orbits, located in the ergoregions, can participate in the processes of extraction of energy from the internal regions of rotating objects, involving an additional vacuum and phantom energy. In the field of spinning solitons, this process can essentially be strengthened by the absence of event horizons [80,86].

Information on the interior structure of a regular rotating black hole can be obtained from the direct observation of its shadow, which presents a black hole image as a dark spot over an image of the remote source of radiation. The shadow boundary is formed by the photon orbits close to their gravitational capture cross section (see [83,87] and the references therein).

A black hole's shadows can be directly observed [88,89], providing information on the black hole's parameters [90,91] and its position and motion with respect to an observer [92]. The Kerr black hole's dependence of the shape of its shadow on its angular momentum and orientation was studied in [91,93,94]. Observational possibilities have been spectacularly demonstrated by the Event Horizon Telescope Collaboration [95], reporting the first observation of a black hole shadow in M 87 [96].

Essential constraints on the nature of a black hole, following from analysis of its shadows, were presented in [91] for several black hole solutions, including those originating from the Bardeen [97] and Hayward [61] spherical solutions.

Photon rings and shadows for the spherical Schwarzschild-MOG black holes have been studied in the frame of the scalar–tensor–vector gravity in [98]. The null geodesics, quasinormal modes and shadows for the Kerr–Newman–Kiselev–Letelier black hole with the equation of the state parameter $w_q = -2/3 = -2/3$ are presented in [99].

In [100], corrections to the photon sphere radius and the black hole shadow due to the cosmological constant were calculated for the standard dark energy action and for the dark energy action related to a Weyl scaling invariant. An investigation of the shadows for non-rotating and rotating charged black holes with scalar Q-hair is presented in [101]. It is shown that charged black holes with scalar Q-hair have smaller shadow sizes than those without Q-hair and that their spin and charge parameters significantly affect the shadow's observables, which allows one to distinguish them from the Reissner–Nordšröm and Kerr–Newmann (KN) black holes.

Current possibilities for testing gravitation theories with black hole shadows were analyzed in [102], as well as for dilaton black holes in [103], for general relativistic transfer in [104], and for hydrodynamical simulations of black hole accretion in [105], which were carried out with the Rezzola–Zhidenko parametrization for general metric theories [106] (for a review, see [107]).

Shadows of de Sitter–Kerr Black Holes

General analysis of the de Sitter–Kerr shadows addressed the questions of the generic difference between their shadows and that for the Kerr black hole and which is dependent on a shadow for the de Sitter–Kerr black hole for its density profile and its angular momentum [108].

Basic equations defining the contour of a shadow: The basic parameters characterizing photon orbits are [83]

$$\xi = L_z/E; \quad \eta = Q/E^2 \tag{21}$$

where E is the integrals of motion related to the Killing vectors $k_t = \delta_t^\alpha$ and L_z is the integral of motion related to the Killing vector $k_\phi = \delta_\phi^\alpha$ in the axially symmetric spacetime (Equation (3)). The integral of motion Q includes the additional quadratic integral of motion $\mathcal{K}$, given by [83]

$$\mathcal{K} = Q + (L_z - aE)^2 \tag{22}$$

which is related to the conformal Killing tensor $K_{\alpha\beta}$, existing in spacetimes of type D according to the Petrov classification (see [83] and the references therein).

The general equations for the null geodesics reads as follows:

$$\frac{\Sigma^2 \dot{r}^2}{E^2} = \mathcal{R}(r) = r^4 + (a^2 - \xi^2 - \eta)r^2 + [\eta + (\xi - a)^2]2\mathcal{M}(r)r - a^2\eta;$$

$$\frac{\Sigma^2 \dot{\theta}^2}{E^2} = \eta + a^2 \cos^2\theta - \xi^2 \cot^2\theta; \quad \frac{\Sigma\dot{\phi}}{E} = \frac{\xi^2}{\sin^2\theta} + \frac{a}{\Delta}[2\mathcal{M}(r)r - a\xi];$$

$$\frac{\Sigma\dot{t}}{E} = -a^2 \sin^2\theta + \frac{1}{\Delta}[(r^2 + a^2)^2 - 2a\mathcal{M}(r)r\xi] \tag{23}$$

where a dot denotes the derivative with respect to the affine parameter along a geodesic.

For the innermost photon orbits $r = const$, they give two equations which define the boundary of the shadow: [108]

$$\mathcal{R}(r) = 0; \quad \partial\mathcal{R}/\partial r = 4r^3 + 2(a^2 - \xi^2 - \eta)r + 2(\mathcal{M} + \mathcal{M}'r)(\eta + (\xi - a)^2 = 0. \tag{24}$$

Identification of a de Sitter–Kerr black hole by its shadow: The celestial coordinates (x, y) are introduced as the impact parameters, shown in Figure 6 (left) [108]. These are related to the orbit parameters (Equation (21)) for the innermost photon orbits, which form the boundary of the gravitational capture cross section, since photons falling in with such impact parameters are captured on the closed innermost orbits [83,87]. The celestial coordinates are defined as follows [108]:

$$x = \rho_\perp = r^2 \sin^2\theta_i \left(\frac{d\phi}{dt}\right)_\infty = \frac{\xi}{\sin\theta_i};$$

$$y = \rho_{||} = r^2 \left(\frac{d\theta}{dt}\right)_\infty = \pm\sqrt{\eta + a^2 \cos^2\theta_i - \xi^2 \cot^2\theta_i}. \tag{25}$$

Here and in Figure 6 (left), θ_i is the angular coordinate of an observer, x is the apparent distance of the black hole image from the symmetry axis orthogonal to it, and y is the apparent distance of its image from the projection on the equatorial plane, which is orthogonal to it.
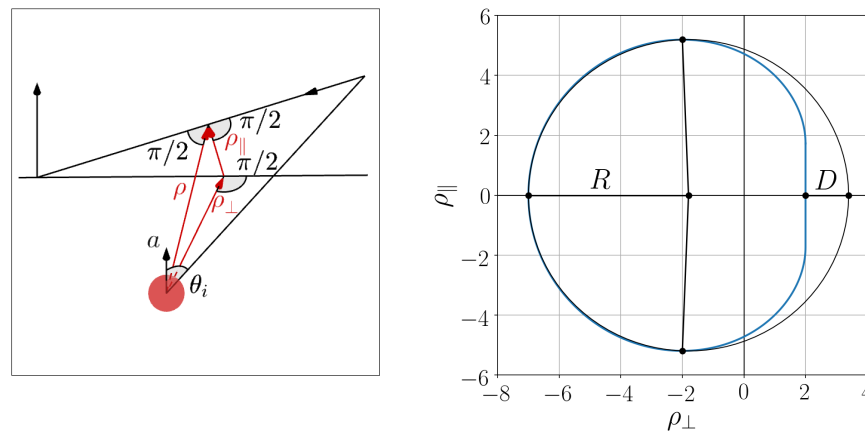
The asymmetry of a shadow contour is determined by introducing a fitting circle of a radius R, with its center denoted by $x = x_C$, and using the coordinates of an upper point of the shadow contour (x_t, y_t) and of its left and right end points in the equatorial plane x_L and x_R, respectively. The asymmetry parameter D is defined [90] as the distance between the right end points of the circle and shadow contour as shown in Figure 6 (right) [108], where $R = x_C - x_L$, $R^2 = (x_C - x_t)^2 + y_t^2$, and $D = 2R - (x_R - x_L)$. Excluding x_C, we obtain the radius of the fitting circle [108]

$$R = \frac{y_t^2 + (x_t - x_L)^2}{2(x_t - x_L)} \tag{26}$$

and the distortion parameter

$$\delta = \frac{D}{R} = 2\left[1 - \frac{(x_R - x_L)(x_t - x_L)}{y_t^2 + (x_t - x_L)^2}\right]. \tag{27}$$

The impact parameters $\rho_\perp$, $\rho_{||}$ (celestial coordinates) and the asymmetry parameter D are shown in Figure 6 (left), where $\rho = \sqrt{\rho_\perp^2 + \rho_{||}^2}$, and in Figure 6 (right), respectively [108].

Figure 6. Impact parameters as celestial coordinates (**left**) and the asymmetry parameter D in the shadow contour (**right**).

The integral of motion $\mathcal{K}$, written in the dimensionless form

$$\mathcal{K} = \eta^2 + (\xi - a)^2, \tag{28}$$

depends on the celestial coordinates as

$$\mathcal{K} = y^2 + (x - as)^2; \; s = \sin \theta_i, \tag{29}$$

which allows one to transform Equation (24) for the shadow contour to the form [108]

$$x = \frac{(-1)}{as(r - f')}\left[r^3 - (4f - f'r)r + a^2 r + a^2 f'\right];$$

$$y^2 = \frac{1}{a^2 s^2 (r - f')^2}\left[4a^2 s^2 r^2 (r^2 - 2f + a^2)\right.$$

$$\left. - \left(r^3 - (4f - f'r)r + a^2(1 + s^2)r + a^2(1 - s^2)f'\right)^2\right] \tag{30}$$

where the distances and mass function are normalized on M, $\mu = \mathcal{M}(r)/M$, and $f = r\mu(r)$.

The derivative dy/dx, which is needed to fix the shadow contour, reads as follows [108]:

$$y\frac{dy}{dx} = \frac{1}{as(r - f')}\left[r^3 - (4f - f'r)r + a^2(1 - s^2)(r + f')\right]. \tag{31}$$

An upper point of the shadow contour $r = r_t$ satisfies $dy/dx = 0$, which gives

$$r_t^3 - (4f_t - f_t'r_t)r_t + a^2(1 - s^2)(r_t + f_t') = 0. \tag{32}$$

$$x_t = -as \cdot \frac{r_t + f_t'}{r_t - f_t'} \qquad y_t^2 = \frac{2r_t}{(r_t - f_t')}\left[r_t^2 + a^2(1 - s^2)\right]. \tag{33}$$

For an observer in the equatorial plane $s = 1$, the orbit equations (Equations (32) and (33)) reduce to

$$r_t - 3\mu_t + \mu_t'r_t = 0; \; x_t = -\frac{2a\mu_t}{r_t - 2\mu_t}; \; y_t^2 = \frac{r_t^3}{r_t - 2\mu_t}. \tag{34}$$

For the Kerr black hole, $\mu(r) = 1$. In addition, $r_t = 3$, $x_t = -2a$, and $y_t^2 = 27$, in agreement with [83].

The left and right points of the shadow contour satisfy equation $y^2 = 0$, where y^2 is given in Equation (30), which defines the shadow contour in the equatorial plane formed by the innermost equatorial orbit as follows:

$$r\left(r[1 + \mu'] - 3\mu\right)^2 + 4a^2\left(r[1 + \mu'] - 3\mu\right) - 4a^2(r - 2\mu) = 0. \tag{35}$$

Its solution gives the radii of the innermost orbits: [108]

$$r_k = \frac{2\mu_k}{1 + \mu'_k}\left[1 - \sqrt{1 - \frac{4\mu'_k}{3}\frac{a^2}{\mu_k^2}}\cos\left(\frac{1}{3}\arccos\left[\frac{1 - 2(1 + \mu'_k)a^2/\mu_k^2}{(1 - 4\mu'_k a^2/3\mu_k^2)^{3/2}}\right] + \frac{2\pi k}{3}\right)\right] \tag{36}$$

where $k = 0, 1, 2$. In the Kerr geometry with $\mu_k = 1$, $\mu'_k = 0$, and Equation (36) gives, in agreement with [83], the following:

$$r_1 = 2\left[1 + \cos\frac{2}{3}\arccos a\right] = r_{ph}^{(-)} \qquad r_2 = 2\left[1 + \cos\frac{2}{3}\arccos(-a)\right] = r_{ph}^{(+)}. \tag{37}$$

It follows that $k = 1$ refers to the retrograde orbit and $k = 2$ refers to the direct orbit. Hence, in an arbitrary axially symmetric geometry, the general solutions in Equation (36) present the retrograde orbits specified by $k = 1$ and the direct orbits specified by $k = 2$.

For an observer in the equatorial plane, Equations (25) and (28) give

$$\xi = x; \qquad \mathcal{K}^2 = (x - a)^2, \tag{38}$$

and the expression for $\mathcal{R}(r)$ in Equation (23) reduces to

$$\mathcal{R}(r) = r\left[r^3 - (x^2 - a^2)r + 2\mu(x - a)^2\right] \tag{39}$$

and obeys the system of equations in Equation (24), which is reduced in turn to

$$r^3 - (x^2 - a^2)r + 2\mu(x - a)^2 = 0; \quad 3r^2 - (x^2 - a^2) + 2\mu'(x - a)^2 = 0 \tag{40}$$

which gives the general constraint on the celestial coordinate x [108]:

$$\frac{x}{a} = \frac{3\mu + (1 - \mu')r}{3\mu - (1 + \mu')r}; \quad \rightarrow \quad \frac{x}{a} < \frac{3\mu + r}{3\mu - r} = \left[\frac{x}{a}\right]_{(Kerr)}, \tag{41}$$

while taking into account that $\mu' \propto \tilde{\rho}$, and hence $\mu' >$ due to $\tilde{\rho} > 0$. The constraint in Equation (41) shows that the shadow of the de Sitter–Kerr black hole is less than that of the Kerr black hole, and the difference depends on its density profile. It also follows that the gravitational capture cross section—which is responsible for the boundary of the black hole shadow—for the de Sitter–Kerr black hole is less than that for the Kerr black hole.

By differentiating x and μ' in Equation (41) and taking into account that $\mu' \propto \tilde{\rho}$ and $\tilde{\rho}' < 0$ for related spherical solutions satisfying the WEC [29], we obtain $dx(3\mu - (1 + \mu')r) \propto -r(x - a)|d\tilde{\rho}|$, which testifies that the difference between a de Sitter–Kerr shadow and a Kerr shadow depends on the pace of the decreasing density profile of the de Sitter–Kerr black hole in that it is lower for a more quickly decreasing density.

A black hole shadow is formed by the innermost photon orbits. The dependence of the shadow of a de Sitter–Kerr black hole on its angular momentum a is determined by the behavior of the curve $r(a)$ for the photon orbits (Equation (18)). In the black hole region, $dr/da < 0$, and the orbit radius decreases with increasing black hole angular momentum a. As a result, the shadow of the de Sitter–Kerr black hole diminishes with increasing values of a. This behavior is illustrated by Figures 7 and 8 below and can be seen as a manifestation of the Lense–Thirring effect (frame dragging).
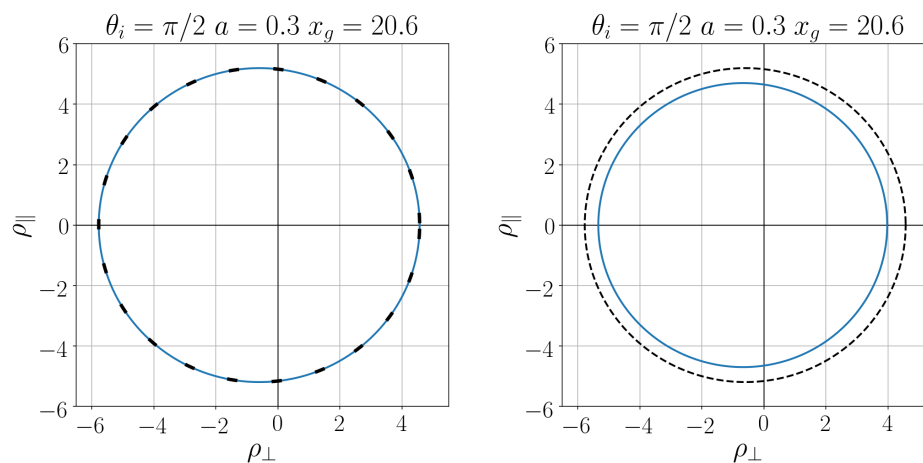
Below, we compare the shadows of a de Sitter–Kerr black hole originating from spherical solutions with different spherical density profiles: one with the phenomenologically regularized Newtonian density profile (Equation (19)) and another with the density profile for the semiclassical model of vacuum polarization in a spherical gravitational field [28]:
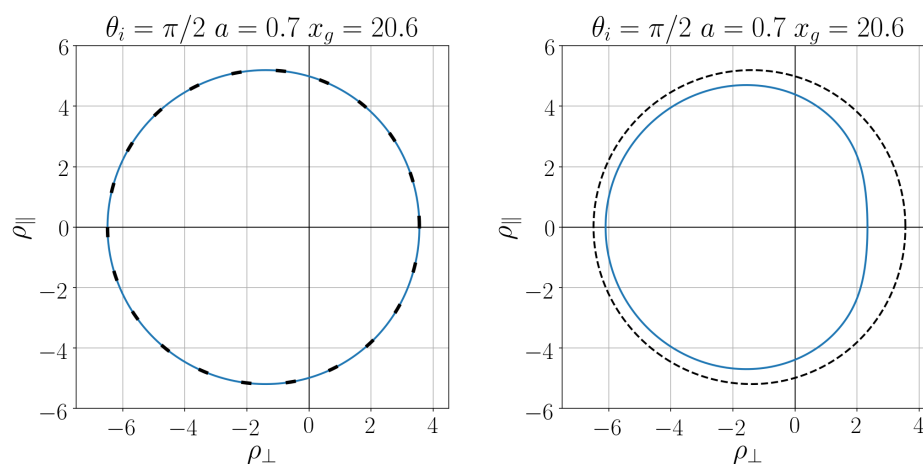
$$\rho(r) = \rho_0 e^{-r^3/r_s^3}; \quad \mathcal{M}(r) = M(1 - e^{-r^3/r_s^3}); \quad r_s = (r_0^2 r_g)^{1/3} \tag{42}$$

which is based on the hypothesis of symmetry restoration at the GUT scale during a gravitational collapse, when all fields contribute to vacuum polarization and thus to gravity via the Einstein equations [28,29,82].

In Figures 7 and 8 [108], we show the shadows of the de Sitter–Kerr black hole compared with that for the Kerr black hole of the same mass, which is plotted with a dashed line, for both density profiles (Equations (19) and (42)), for two values of the angular momentum a. The angle θ_i is the angular coordinate of an observer. The characteristic parameter of the de Sitter–Kerr geometry $x_g = r_g/r_0$ is chosen to be $x_g = 20.06$.

Figure 7. Comparison of shadows for the quickly decreasing density (Equation (42)) (**left**) and for the slowly decreasing density (Equation (19)) (**right**) for $a = 0.3$. The observer angular coordinate $\theta_i = \pi/2$.

Figure 8. Comparison of shadows for the quickly decreasing density (Equation (42)) (**left**) and for the slowly decreasing density (Equation (19)) (**right**) for $a = 0.7$. The observer angular coordinate $\theta_i = \pi/2$.

The difference between the de Sitter–Kerr shadow and the Kerr shadow was more significant for the slowly decreasing density (Equation (19)) than for the quickly falling

density (Equation (42)), which demonstrates the essential dependence of the shadow boundary on the pace of the decrease in density [108].

The shadows of the black holes, shown in Figures 7 and 8 differed first by the profile for the pace of the decreasing density of the de Sitter–Kerr black hole. For the quickly decreasing density (Equation (42)), the shadow of the de Sitter–Kerr black hole practically coincided with that of the Kerr black hole. Second, the shadow of the de Sitter–Kerr black hole diminished with an increase in the black hole's angular momentum.

5. Conclusions

The limiting orbits, presented by the innermost particle and photon orbits, provided the most informative diagnostic tool for investigating regular de Sitter–Kerr black holes and solitons.

De Sitter–Kerr black holes and solitons are confined by light rings, which are their basic constituents formed by the closed photon orbits. This fact identifies them as ultra-compact objects, defined as the self-gravitating systems with the light rings [81].

Around a de Sitter–Kerr black hole, there exists one co-rotating light ring and one counter-rotating light ring, in agreement with the results reported in [78] that co-rotating and counter-rotating light rings "always appear in pairs". However, the spinning solitons displayed a more interesting picture: one counter-rotating light ring and up to four co-rotating light rings. The innermost light rings around de Sitter–Kerr solitons are stable [80].

Direct information about the basic characteristic parameters of a rotating black is obtained from observations of its shadow, whose boundary is formed by photons captured on the innermost photon orbits. The detailed analysis of general dynamical equations for de Sitter–Kerr shadows has shown the following: (1) The shape of the shadow for de Sitter–Kerr black hole depends essentially on the form of its density profile. (2) The shadow of the de Sitter–Kerr black hole is less than that for the Kerr black hole of the same mass. (3) The gravitational capture cross section, which is responsible for the boundary of the black hole shadow, as that of the de Sitter–Kerr black hole is less than that for the Kerr black hole. (4) The difference essentially depends on the pace the decrease in the density profile of the de Sitter–Kerr black hole, which occurs much less for a quickly decreasing density than for a density decreasing slowly. (5) The shadow for the de Sitter–Kerr black hole decreases, and its difference with the Kerr shadow increases with an increase in the angular momentum a [108].

One can expect that the comparison of an observed black hole shadow with that for a Kerr black hole of the same mass and restoring its density profile from the observed shadow would give a certain information about the nature of its interior content.

Collisions of particles in the innermost orbits with particles on unbound orbits, when crossing phantom regions, can boost energy output from the deep interiors of de Sitter–Kerr ultra-compact objects by involving de Sitter or phantom energy. For spinning solitons, the processes of energy extraction should be more efficient due to absence of the event horizons [54,80].

References

1. Anderson, L.; Aubourg, E.; Bailey, S.; Beutler, F.; Bhardwaj, V.; Blanton, M.; Bolton, A.S.; Brinkmann, J.; Brownstein, J.R.; Burden, A.; et al. The clustering of galaxies in the SDSS-III Baryon Oscillation Spectroscopic Survey: Baryon acoustic oscillations in the Data Releases 10 and 11 Galaxy samples. *Mon. Not. R. Astron. Soc.* **2014**, *441*, 24–62. [CrossRef]
2. Rivera, A.B.; Garcia-Farieta, J.E. Exploring the Dark Universe: Constraint on dynamical dark energy models from CMB, BAO and Growth Rate Measurements. *Int. J. Mod. Phys. D* **2019**, *28*, 1950118. [CrossRef]
3. Olive, K. Inflation. *Phys. Rep.* **1990**, *190*, 309–403. [CrossRef]
4. Bassett, B.A.; Kunz, M.; Silk, J.; Ungarelli, C. A late-time transition in the cosmic dark energy? *Mon. Not. R. Astron. Soc.* **2002**, *336*, 1217–1222. [CrossRef]
5. Corasaniti, P.S.; Kunz, M.; Parkinson, D.; Copeland, E. J.; Bassett, B.A. Foundations of observing dark energy dynamics with the Wilkinson Microwave Anisotropy Probe. *Phys. Rev. D* **2004**, *70*, 083006:1–083006:15. [CrossRef]
6. Ade, P.A.; Aikin, R.W.; Barkats, D.; Benton, S.J.; Bischoff, C.A.; Bock, J.J.; Bicep2 Collaboration. Detection of B-Mode Polarization at Degree Angular Scales by BICEP2. *Phys. Rev. Lett.* **2014**, *112*, 241101:1–241101:25. [CrossRef] [PubMed]
7. Perlmutter, S.; Aldering, G.; Goldhaber, G.; Knop, R.A.; Nugent, P.; Castro, P.G.; Deustua, S.; Fabbro, S.; Goobar, A.; Groom, D.E. Measurements of Ω and $\wedge$ from 42 High-Redshift Supernovae. *Astrophys. J.* **1999**, 517, 565–586. [CrossRef]
8. Suzuki, N.; Rubin, D.; Lidman, C.; Aldering, G.; Amanullah, R.; Barbary, K.; Supernova Cosmology Project. The Hubble Space Telescope Cluster Supernova Survey: Improving the Dark Energy Constraints and Building an Early-Type-Hosted Supernova Sample. *Astrophys. J.* **2012**, *746*, 85–109. [CrossRef]
9. Nojiri, S.; Odintsov, S.D. Introduction to modified gravity and gravitational alternative for dark energy. *Int. J. Mod. Phys.* **2007**, *4*, 115–145. [CrossRef]
10. De Felice, A.; Tsujikawa, S. $f(R)$ Theories. *Living Rev. Relativ.* **2010**, *13*, 3.
11. Nojiri, S.I.; Odintsov, S.D. Unified cosmic history in modified gravity: From $F(R)$ theory to Lorentz non-invariant models. *Phys. Rep.* **2011**, *505*, 59–144. [CrossRef]
12. Bamba, K.; Capozziello, S.; Nojiri, S.; Odintsov, S.D. Dark energy cosmology: The equivalent description via different theoretical models and cosmography tests. *Astrophys. Sp. Sci.* **2012**, *342* 155–228. [CrossRef]
13. Sahni, V.; Shafiello, A.; Starobinsky, A.A. Model-independent Evidence for Dark Energy Evolution from Baryon Acoustic Oscillations. *Astrophys. J.* **2014**, *793*, L40–L44. [CrossRef]
14. Gliner, E.B.; Dymnikova, I.G. Nonsingular Friedmann cosmology. *Sov. Astron. Lett.* **1975**, *1*, 93–95.
15. Bronnikov, K.A.; Dobosz, A.; Dymnikova, I. Nonsingular vacuum cosmologies with a variable cosmological term. *Class. Quant. Grav.* **2003**, *20*, 3797–3814. [CrossRef]
16. Bronnikov, K.A.; Dymnikova, I. Regular homogeneous T-models with vacuum dark fluid. *Class. Quant. Grav.* **2007**, *24*, 5803–5816. [CrossRef]
17. Bronnikov, K.A.; Dymnikova, I.; Galaktionov, E. Multihorizon spherically symmetric spacetimes with several scales of vacuum energy. *Class. Quant. Grav.* **2012**, *29*, 095025:1–0950:22. [CrossRef]
18. Dymnikova, I.; Dobosz, A.; Sołtysek, B. Lemaître Class Dark Energy Model for Relaxing Cosmological Constant. *Universe* **2017**, *3*, 39. [CrossRef]
19. Dymnikova, I.; Dobosz, A. Spacetime Symmetry and LemaîTre Class Dark Energy Models. *Symmetry* **2019**, *11*, 90. [CrossRef]
20. Dymnikova, I. The algebraic structure of a cosmological term in spherically symmetric solutions. *Phys. Lett. B* **2000**, *472*, 33–38. [CrossRef]
21. Dymnikova, I.; Galaktionov, E. Vacuum dark fluid. *Phys. Lett. B* **2007**, *645*, 358–364. [CrossRef]
22. Dymnikova, I.; Galaktionov, E. Dark ingredients in one drop. *Central Europ. J. Phys.* **2011**, *9*, 644–653. [CrossRef]
23. Coleman, S. Classical lumps and their quantum descendants. In *New Phenomena in Subnuclear Physics*; Zichichi, A., Ed.; Plenum: New York, NY, USA, 1977; p. 297.
24. Dymnikova, I. Dark Energy and Spacetime Symmetry. *Universe* **2017**, *3*, 20. [CrossRef]
25. Anderson, P.R. Attractor states and infrared scaling in de Sitter space. *Phys. Rev. D* **2000**, *62*, 124019:1–124019:30. [CrossRef]
26. Petrov, A.Z. *Einstein Spaces*; Pergamon Press: Oxford, UK, 1969.
27. Stephani, H.; Kramer, D.; MacCallum, V.; Hoenselaers, C.; Herlt, E. *Exact Solutions of Einstein's Field Equations*; Cambridge University Press: Cambridge, UK, 2003.
28. Dymnikova, I. Vacuum nonsingular black hole. *Gen. Rel. Grav.* **1992**, *24*, 235–242. [CrossRef]
29. Dymnikova, I. The cosmological term as a source of mass. *Class. Quant. Grav.* **2002**, *19*, 725–740. [CrossRef]
30. Dymnikova, I. Spherically symmetric space-time with regular de Sitter center. *Int. J. Mod. Phys. D* **2003**, *12*, 1015–1034. [CrossRef]
31. Poisson, E.; Israel, W. Structure of the black hole nucleus. *Class. Quant. Grav.* **1988**, *5*, L201–L205. [CrossRef]
32. Frolov, V.P.; Markov, M.A.; Mukhanov, V.F. Black holes as possible sources of closed and semiclosed worlds. *Phys. Rev. D* **1990**, *41*, 383–394. [CrossRef]
33. Dymnikova, I. Internal structure of nonsingular spherical black holes. In *Internal Sructure of Black Holes and Spacetime Singularities*; Burko, M., Ori, A., Eds.; Annals of the Israel Physical Society; Bristol Insitute of Physics Pulishing: Bristol, UK; Philadelphia, PA, USA; Jerusalem, Israel, 1997; Volume 13, pp. 422–440.
34. Perez, A. Spin foam models for quantum gravity. *Class. Quant. Grav.* **2003**, *20*, R43–R104. [CrossRef]
35. Rovelli, C. *Quantum Gravity*; Cambridge University Press: Cambridge, UK, **2004**.

36. Bonanno, A.; Reuter, M. Spacetime structure of an evaporating black hole in quantum gravity. *Phys. Rev. D* **2006**, *73*, 083005–083017. [CrossRef]
37. Nicolini, P. Noncommutative black holes, the final appeal to quantum gravity: A review. *Int. J. Mod. Phys. A* **2009**, *24*, 1229–1308. [CrossRef]
38. Kerr, R.P.; Schild, A. Some algebraically degenerate solutions of Einstein's gravitational field equations. *Proc. Symp. Appl. Math.* **1965**, *17*, 199.
39. Gürses, M.; Gürsey, F. Lorentz covariant treatment of the Kerr-Schild geometry. *J. Math. Phys.* **1975**, *16*, 2385–2390. [CrossRef]
40. Newman, E.T.; Janis, A.J. Note on the Kerr Spinning Particle Metric. *J. Math. Phys.* **1965**, *6*, 915–917. [CrossRef]
41. Iso, S.; Umetsu, H.; Wilczek, F. Anomalies, Hawking radiations, and regularity in rotating black holes. *Phys. Rev. D* **2006**, *74*, 044017. [CrossRef]
42. Caravelli, F.; Modesto, L. Spinning loop black holes. *Class. Quant. Grav.* **2010**, *27*, 245022. [CrossRef]
43. Bambi, C.; Modesto, L. Rotating regular black holes. *Phys. Lett. B* **2013**, *721*, 329–334. [CrossRef]
44. Balart, L.; Vagenas, E.C. Regular black hole metrics and the weak energy condition. *Phys. Lett. B* **2014**, *730*, 14–17. [CrossRef]
45. Toshmatov, B.; Ahmedov, B.; Abdujabbarov, A.; Stuchlik, Z. Rotating regular black hole solution. *Phys. Rev. D* **2014**, *89*, 104017. [CrossRef]
46. Neves, J.C.S.; Saa, A. Regular rotating black holes and the weak energy condition. *Phys. Lett. B* **2014**, *734*, 44–48. [CrossRef]
47. Ghosh, S.G. A nonsingular rotating black hole. *Eur. Phys. J. C* **2015**, *75*, 532. [CrossRef]
48. Takeuchi, S. Hawking fluxes and Anomalies in Rotating Regular Black Holes with a Time-Delay. *Class. Quant. Grav.* **2016**, *33*, 225016. [CrossRef]
49. de Lorenzo, T.; Giusti, A.; Speziale, S. Non-singular rotating black hole with a time delay in the center. *Gen. Rel. Grav.* **2016**, *48*, 31. [CrossRef]
50. Torres, R.; Fayos, F. On regular rotating black holes. *Gen. Rel. Grav.* **2017**, *49*, 2. [CrossRef]
51. Dymnikova, I.; Galaktionov, E. Basic Generic Properties of Regular Rotating Black Holes and Solitons. *Adv. Math. Phys.* **2017**, *2017*, 1035381. [CrossRef]
52. Dymnikova, I. Spinning self-gravitating electrovacuum soliton. *Phys. Lett. B* **2006**, *639*, 368–372. [CrossRef]
53. Dymnikova, I.; Galaktionov, E. Regular rotating electrically charged black holes and solitons in nonlinear electrodynamics minimally coupled to gravity. *Class. Quant. Grav.* **2015**, *32*, 165015. [CrossRef]
54. Dymnikova, I.; Galaktionov, E. Regular rotating de Sitter-Kerr black holes and solitons. *Class. Quant. Grav.* **2016**, *33*, 145010. [CrossRef]
55. Dymnikova, I. Dark Matter Candidates with Dark Energy Interiors Determined by Energy Conditions. *Symmetry* **2020**, *12*, 662. [CrossRef]
56. Caldwell, R.R. A phantom menace? Cosmological consequences of a dark energy component with super-negative equation of state. *Phys. Lett. B* **2002**, *545*, 23–29. [CrossRef]
57. Bronnikov, K.A.; Rubin, S.G. *Black Holes, Cosmology and Extra Dimensions*; World Scientific: Singapore, 2013.
58. Schnittman, J.D. The Collisional Penrose Process. *Gen. Rel. Grav.* **2018**, *50*, 77. [CrossRef] [PubMed]
59. Toshmatov, B.; Abdujabbarov, A.; Ahmedov, B.; Stuchlik, Z. Particle motion and Penrose processes around rotating regular black hole. *Astroph. Sp. Sci.* **2015**, *357*, 41. [CrossRef]
60. Toshmatov, B.; Stuchlik, Z.; Ahmedov, B. Generic rotating regular black holes in general relativity coupled to nonlinear electrodynamics. *Phys. Rev. D* **2017**, *95*, 084037. [CrossRef]
61. Hayward, S.A. Formation and evaporation of non-singular black holes. *Phys. Rev. Lett.* **2006**, *96*, 031103. [CrossRef]
62. Chiba, T.; Kimura, M. A note on geodesics in the Hayward metric. *Prog. Theor. Exp. Phys.* **2017**, *2017*, 043E01. [CrossRef]
63. Bautista-Olvera, B.; Degollado, J.C.; German, G. Geodesic structure of a rotating regular black hole. *arXiv* **2019**, arXiv:1908.01886.
64. Teo, E. Spherical orbits around a Kerr black hole. *Gen. Rel. Grav.* **2021**, *53*, 10. [CrossRef]
65. Cao, W.; Liu, W.; Wu, X. Integrability of Kerr-Newman spacetime with cloud strings, quintessence and electromagnetic field. *Phys. Rev. D* **2022**, *105*, 124039. [CrossRef]
66. Zhang H.; Zhou, N.; Liu, W.; Wu, X. Charged Particle Motions near Non-Schwarzschild Black Holes with External Magnetic Fields in Modified Theories of Gravity. *Universe* **2021**, *7*, 488. [CrossRef]
67. Yang, D.; Cao, W.; Zhou, N.; Zhang, H.; Liu, W.; Wu, X. Chaos in a Magnetized Modified Gravity Schwarzschild Spacetime. *Universe* **2022**, *8*, 320. [CrossRef]
68. Wang, Y.; Sun, W.; Liu, F.; Wu, X. Construction of Explicit Symplectic Integrators in General Relativity. III. Reissner-Nordström-(anti)-de Sitter Black Holes. *Astrophys. J. J. Suppl. Ser.* **2021**, *254*, 8. [CrossRef]
69. Zhang, H.; Zhou, N.; Liu, W.; Wu, X. Equivalence between two charged black holes in dynamics of orbits outside the event horizons. *Gen. Rel. Grav.* **2022**, *54*, 110. [CrossRef]
70. Teo, E. Spherical Photon Orbits Around a Kerr Black Hole. *Gen. Rel. Grav.* **2003**, *35*, 1909–1926. [CrossRef]
71. Johannsen, T. Photon rings around Kerr and Kerr-like black holes. *Astrophys. J.* **2013**, *777*, 170. [CrossRef]
72. Mokdad, M. Reissner-Nordstrøm-de Sitter Manifold: Photon Sphere and Maximal Analytic Extension. *arXiv* **2017**, arXiv:1701.06982.
73. Dolan, S.R.; Shipley, J.O. Stable photon orbits in stationary axisymmetric electrovacuum spacetimes. *Phys. Rev. D* **2016**, *94*, 044038. [CrossRef]

74.	Hod, S. On the number of light rings in curved spacetimes of ultra-compact objects. *Phys. Lett. B* **2018**, *776*, 1–4. [CrossRef]
75.	Hod, S. Analytic study of self-gravitating polytropic spheres with light rings. *Eur. Phys. J. C* **2018**, *78*, 417. [CrossRef]
76.	Cunha, P.V.P.; Berti, E.; Herdeiro, C.A.R. Light-Ring Stability for Ultracompact Objects. *Phys. Rev. Lett.* **2017**, *119*, 251102. [CrossRef]
77.	Cunha, P.V.P.; Herdeiro, C.A.R. Stationary Black Holes and Light Rings. *Phys. Rev. Lett.* **2020**, *124*, 181101. [CrossRef] [PubMed]
78.	Guo, M.; Gao, S. Universal properties of light rings for stationary axisymmetric spacetimes. *Phys. Rev. D* **2021**, *103*, 104031. [CrossRef]
79.	Ghosh, R.; Sarkar, S. Light rings of stationary spacetimes. *Phys. Rev. D* **2021**, *104*, 044019. [CrossRef]
80.	Dymnikova, I.; Dobosz, A.; Sołtysek, B. Classification of Circular Equatorial Orbits around Regular Rotating Black Holes and Solitons with the de Sitter/Phantom Interiors. *Universe* **2022**, *8*, 65. [CrossRef]
81.	Cardoso, V.; Crispino, L.C.B.; Macedo, C.F.B.; Okawa, H.; Pani, P. Light rings as observational evidence for event horizons: Long-lived modes, ergoregions and nonlinear instabilities of ultracompact objects. *Phys. Rev. D* **2014**, *90*, 044069. [CrossRef]
82.	Dymnikova, I. De Sitter-Schwarzschild black hole: Its particlelike core and thermodynamical properties. *Int. J. Mod. Phys. D* **1996**, *5*, 529–540. [CrossRef]
83.	Chandrasekhar, S. *The Mathematical Theory of Black Holes*; Clarendon Press: Oxford, UK, 1983.
84.	Dymnikova, I. Mass, Spacetime Symmetry, de Sitter Vacuum, and the Higgs Mechanism. *Symmetry* **2020**, *12*, 634. [CrossRef]
85.	Dymnikova, I.; Khlopov, M. Regular black hole remnants and graviatoms with de Sitter interior as heavy dark matter candidates probing inhomogeneity of early universe. *Int. J. Mod. Phys. D* **2015**, *24* 1545002. [CrossRef]
86.	Dymnikova, I. The Fundamental Roles of the de Sitter Vacuum. *Universe* **2020**, *6*, 101. [CrossRef]
87.	Dymnikova, I.G. Motion of particles and photons in the gravitational field of a rotating body. *Sov. Phys. Uspekhi* **1986**, *29*, 215–237. [CrossRef]
88.	Falcke, H.; Melia, F.; Agol E. Viewing the shadow of the black hole at the Galactic Center. *Astrophys. J. Lett.* **2000**, *528*, L13–L16. [CrossRef] [PubMed]
89.	Takahashi, R. Shapes and positions of black hole shadows in accretion disks and spin parameters of black holes. *Astrophys. J.* **2004**, *611*, 996–1004. [CrossRef]
90.	Hioki, K.; Maeda, K. Measurement of the Kerr spin parameter by observation of a compact object's shadow. *Phys. Rev. D* **2009**, *80*, 024042. [CrossRef]
91.	Li, Z.; Bambi, C. Measuring the Kerr spin parameter of regular black holes from their shadow. *J. Cosmol. Astropart. Phys.* **2014** *2014*, 041–061. [CrossRef]
92.	Mars, K.; Paganini, C.F.; Oancea, M.A. The fingerprints of black holes - shadows and their degeneracies. *Class. Quant. Grav.* **2018**, *35*, 025005. [CrossRef]
93.	Grenzebach, A.; Perlick, V.; Lämmerzahl, C. Photon regions and shadows of Kerr-Newman-NUT black holes with a cosmological constant. *Phys. Rev. D* **2014**, *89*, 124004. [CrossRef]
94.	Repin, S.V.; Kompaneets, D.A.; Novikov, I.D.; Mityagina, V.A. Shadow of rotating black holes on a standard background screen.*arXiv* **2018**, arXiv:1802.04667.
95.	Doeleman, S.S.; Weintroub, J.; Rogers, A.E.; Plambeck, R.; Freund, R.; Tilanus, R.P.; Woody, D. Event-horizon-scale structure in the supermassive black hole candidate at the Galactic Center. *Nature* **2008**, *455*, 78–80. [CrossRef]
96.	The Event Horizon Telescope Collaboration. First M87 Event Horizon Telescope Results. I. The Shadow of the Supermassive Black Hole. *Astrophys. J. Lett.* **2019**, *875*, L1–L8. [CrossRef]
97.	Ayon-Beato, A.; Garcia, A. The Bardeen model as a nonlinear magnetic monopole. *Phys. Lett. B* **2000**, *493*, 149–152. [CrossRef]
98.	Hu, S.; Deng, C.; Wu, X.; Liang, E. Observational signatures of Schwarzschild-MOG black holes in scalar-tensor-vector gravity: Shadows and rings with different accretions. *Eur. Phys. J. C* **2022**, *82*, 885. [CrossRef]
99.	Atamurotov, F.; Hussain, I.; Mustafa, G.; Jusufi, K. Shadow and quasinormal modes of the Kerr–Newman–Kiselev–Letelier black hole. *Europ. Phys. J. C* **2022**, *82*, 831. [CrossRef]
100.	Adler, S.L.; Virbhadra, K.S. Cosmological constant corrections to the photon sphere and black hole shadow radii. *Gen. Rel. Grav.* **2022**, *54*, 93. [CrossRef]
101.	Wu, M.-H.; Guo, H.; Kuang, X.-M. Shadow Cast of Rotating Charged Black Hole with Scalar Q-Hair. *Symmetry* **2022**, *14*, 2237. [CrossRef]
102.	Mizuno, Y.; Younsi, Z.; Fromm, C.M.; Porth, O.; De Laurentis, M.; Olivares, H.; Falcke, H.; Kramer, M.; Rezzolla, L. The current ability to test theories of gravity with black hole shadows. *Nat. Astron. Lett.* **2018**, *2*, 585–590. [CrossRef]
103.	Garca, A.; Galtsov, D.; Kechkin, O. Class of stationary axisymmetric solutions of the Einstein-Maxwell-dilaton-axion field equations. *Phys. Rev. Lett.* **1995**, *74*, 1276–1279. [CrossRef] [PubMed]
104.	Mizuno, Y.; Younsi, Z.; Wu, K.; Fuerst, S.V. General relativistic radiative transfer: Formulation and emission from structured tori around black holes. *Astron. Astrophys.* **2012**, *545*, A13.
105.	Chan, C.-K.; Psaltis, D.; Oezel, F.; Narayan, R.; Sadowski, A. The power of imaging: Constraining the plasma properties of GRMHD simulations using EHT observations of Sgr A. *Astrophys. J.* **2015**, *799*, 1. [CrossRef]
106.	Rezzolla, L.; Zhidenko, A. New parametrization for spherically symmetric black holes in metric theories of gravity. *Phys. Rev. D* **2014**, *90*, 084009. [CrossRef]

107. Cunha, P.V.P.; Herdeiro, C.A.R. Shadows and strong gravitational lensing: A brief review. *Gen. Rel. Grav.* **2018**, *50*, 42–51. [CrossRef]

108. Dymnikova, I.; Kraav, K. Identification of a Regular Black Hole by Its Shadow. *Universe* **2019**, *5*, 163. [CrossRef]